

Article

# Enhanced Heat Transfer in Moderately Ionized Liquid Due to Hybrid MoS<sub>2</sub>/SiO<sub>2</sub> Nanofluids Exposed by Nonlinear Radiation: Stability Analysis

Umair Khan <sup>1</sup>, A. Zaib <sup>2</sup>, Ilyas Khan <sup>3,\*</sup>, Dumitru Baleanu <sup>4,5,6</sup> and Kottakkaran Sooppy Nisar <sup>7</sup>

<sup>1</sup> Department of Mathematics and Social Sciences, Sukkur IBA University, Sukkur 65200, Sindh, Pakistan

<sup>2</sup> Department of Mathematical Sciences, Federal Urdu University of Arts, Science & Technology, Gulshan-e-Iqbal, Karachi 75300, Pakistan

<sup>3</sup> Faculty of Mathematics and Statistics, Ton Duc Thang University, Ho Chi Minh City 72915, Vietnam

<sup>4</sup> Department of Mathematics, Cankaya University, 06790 Ankara, Turkey

<sup>5</sup> Institute of Space Sciences, 077125 Magurele, Romania

<sup>6</sup> Department of Medical Research, China Medical University Hospital, China Medical University, Taichung 404, Taiwan

<sup>7</sup> Department of Mathematics, College of Arts and Sciences, Prince Sattam bin Abdulaziz University, Wadi Aldawaser 11991, Saudi Arabia

\* Correspondence: ilyaskhan@tdtu.edu.vn

Received: 10 January 2020; Accepted: 20 February 2020; Published: 24 February 2020



**Abstract:** This study considers ethylene-glycol as a moderate ionized regular liquid whose rheological behavior can be analyzed through the relations of the Carreau stress–strain tensor. Hybrid nanoliquids are potent liquids that give better performance for heat transfer and the properties of thermo physical than regular heat transfer liquids (water, ethylene glycol, and oil) and nanoliquids by single nanomaterials. Here, a type of hybrid nanoliquid involving silicon oxide (SiO<sub>2</sub>) and Molybdenum disulfide (MoS<sub>2</sub>) nanoparticles with ethylene glycol as a base liquid are considered. In addition, the impact of nonlinear radiation along with Lorentz force is invoked. Similarity variables are utilized to acquire the numerical findings and their solutions for transmuting ordinary differential equations (ODEs). Using `bvp4c` from MATLAB, we can obtain these quantitative and numerical results of the converted nonlinear equations. The impacts of the pertinent constraints on the temperature distribution, velocity, Nusselt number, and skin friction are estimated. The outcomes indicate that the double-edged methods for the results originate from the precise values of the permeable parameters. Further, the critical values ( $S_c = 1.9699, 2.0700$  and  $2.2370$ ) are enhanced due to the influence of the local Weissenberg number. This implies that the increasing value of the local Weissenberg number accelerate the boundary layer separation. Furthermore, a stability investigation is performed and confirms that the first solution is a physically reliable solution.

**Keywords:** Magnetohydrodynamic flow; generalized Carreau fluid; shrinking sheet; radiative heat transfer

## 1. Introduction

Hybrid nanoliquids are an extraordinary group of heat transport liquids. These liquids are technologically created to increase the performance of heat transport in several engineering and industrial processes. A hybrid nanoliquid is prepared by dispersing two distinct nanomaterials. This new class of nanoliquid offers improved thermal effectiveness compared to a conventional nanoliquid and a regular liquid. The optimization of the efficiency of this nanoliquid's thermal

system is critical in numerous scientific applications, such as in the cooling systems of automobiles, micro-electronics, power generation, acoustics, air conditioning, heat exchangers, etc. Thus, it is vital to manage the thermal conductivity of this type of liquid to ensure a better performance of heat transport. Sarkar et al. [1] and Sidik et al. [2] summarized the current research related to the preparation techniques for hybrid nanoliquids, the thermo-physical properties of hybrid nanoliquids, and the recent applications of hybrid nanoliquids. The expansion of hybrid nanoliquids, along with improved thermal conductivity and admirable stability, is indispensable and can help guide us to optimize energy and make it more sustainable, since hybrid nanoliquids enhance the thermal system's efficiency, as reviewed by Das [3]. Ghadikolaie et al. [4] discussed the influence of the magnetic number on a stagnation-point flow consisting of water-based Cu and TiO<sub>2</sub> hybrid nanoparticles from a stretched sheet using shape factors. Zeeshan et al. [5] presented an analytic result for the Poiseuille flow involving a C<sub>2</sub>H<sub>6</sub>O<sub>2</sub>/Al<sub>2</sub>O<sub>3</sub> nanoliquid through a wavy porous channel. The impacts of thermal radiation and shape factor into the 3D flow of a heat transport containing water and an ethylene glycol-based Ag/Fe<sub>3</sub>O<sub>3</sub> hybrid nanoliquid from a rotated stretched channel, as demonstrated by Ghadikolaie et al. [6]. Khan et al. [7] scrutinized the influence of binary reactions on a magnetic-radiative cross flow involving Ti<sub>6</sub>Al<sub>4</sub>V nanomaterials with activation energy and presented multiple solutions. Recently, Kumar and Sahoo [8] analyzed the viscosity and thermal conductivity of a propylene glycol and ethylene glycol-based CuO\Al<sub>2</sub>O<sub>3</sub> nanoliquid along with different-shaped nanomaterials. They also analyzed the X-ray diffraction and zeta potential.

Presently, a great deal of curiosity has been exhibited by researchers to vet the flow of a type of fluid with the characteristics of heat transfer due to a shrinking surface. A sheet that shrinks in size by applying a suction or external heat is called a shrinking sheet. The common applications that involve a shrinking surface are called shrinking films. The aforementioned films are instrumental in wrapping products in huge amounts since they can be easily removed with the help of sufficient heat. Problems involving shrinking films can be used to investigate the impact of capillaries in the minor pores, the behavior of the shrinking-swell, and the characteristics of hydraulic agricultural clay soils. Wang [9] developed a viscous flow towards a shrinking surface. Miklavčič and Wang [10] recognized the uniqueness and existence criteria for the problem of a viscous flow by using suction. A steady MHD viscous flow past a decreasing surface with suction was vetted by Fang and Zhang [11]. Khan et al. [12] discussed the influence of variable viscosity on a laminar thin film flow through a stretching/shrinking sheet in the presence of erratic thermal conductivity. Bhattacharyya et al. [13] investigated the point at which the motion of a fluid is zero at the boundary layer with the properties of transfer of heat from the shrinking surface with a partial slip effect. Makinde et al. also examined an MHD mix convection flow containing a nanoliquid near the point of stagnation towards a sheet that is convectively heated and stretched [14]. The steady electric conducting viscous flow past a porous shrinking surface with second-order slip effect was scrutinized by Mahmood et al. [15]. Mansur et al. [16] explored the flow of the stagnation point under the assumption of an MHD containing a nanofluid at an ambient point past a penetrable expanding/contracting sheet.

The aforementioned research is confined to Newtonian fluids. However, several industrial fluids have been studied, such as muds, artificial fibers, condensed milk, slurries, polymeric fluids, sugar solutions, foods, banana puree, and blood show. These fluids show the behaviors of non-Newtonian liquids. Modelling these non-Newtonian fluids presents a variety of challenges to researchers. Therefore, it is imperative to consider the characteristics of heat transfer in non-Newtonian fluids from a pragmatic viewpoint. Many researchers have introduced numerous models for that do not agree with the Newtonian law and are thus called non-Newtonian fluids. One of these non-Newtonian liquids or wide-ranging Newtonian fluids is called "Carreau." In 1972, Carreau [17] introduced the global range of a fluid, a non-Newtonian fluid and called it a "Carreau" fluid. This Carreau model reasonably coincides with the behavior of polymer suspensions under various flow conditions. This perfect scheme is especially suited to promoting dilutions, polymers, and aqueous solutions and dissolutions. The present model also explains the shear weakening and shear congealing performances of several

non-Newtonian liquids. MHD flow was investigated by Akbar et al. [18] at the stagnation-point of a Carreau fluid past a leaky contracting surface; the study acquired multiple results. The Hall effects in an MHD Carreau Yasuda liquid with peristaltic transport through the curved channel were discussed by Abbasi et al. [19]. Masood and Hashim [20] examined a one-dimensional viscous flow with the characteristics of heat transfer involving a Carreau liquid from a stretched sheet that is considered to be non-linear. Masood et al. [21] studied the impact of radiation, which is considered to be non-linear for the MHD flow of a Carreau liquid from the expanded sheet under a convective boundary condition that is also considered nonlinear.

Thus, convective conditions with thermal radiation are evident in manufacturing and engineering processes, and their impacts can be seen in those fields. Gas and nuclear turbines, chemical reactions, and lye forging are a few examples. Aziz [22] discussed the influence of the convective boundary conditions of the flow from a flat plate. MHD flow with the properties of heat transfer has been scrutinized by Makinde [23] together with mixed convection, thereby creating a plate engrossed in permeable medium with convective boundary conditions. The boundary layer and heat transfer flow from a spongy expanded surface through a convective boundary condition were numerically examined by Ishak [24]. A mixed convective flow was studied by Rahman et al. [25], who considered the impact of the convective boundary condition through a vertical plate. Ibrahim and Haq [26] examined the electric conducting flow comprising a nano-liquid near the point where the velocity is taken to be zero over the expanded sheet through a convective condition. Makinde et al. [27] investigated the impact of slip on the electric conducting flow near the ambient position where the fluid is flowing at infinity and contains a nano-liquid from a convective heated expanded surface with a radiation effect.

In summary, the aim of the present study is to analyze the MHD flow with the characteristics of heat transfer involving a partially ionized non-Newtonian Carreau liquid through hybrid nanoliquids from a shrinking sheet under convective conditions and nonlinear thermal radiation. A hybrid nanoliquid is numerically created by suspending two distinct nanomaterials, Silicon dioxide ( $\text{SiO}_2$ ) (using sand) and Molybdenum disulfide ( $\text{MoS}_2$ ). In addition, water is used as the regular liquid. Moreover, Molybdenum is a chemical factor and does not occur physically as a free metal on Earth. It is only observed in the structures of oxides. The existence of  $\text{MoS}_2/\text{SiO}_2$  nanomaterials with ethylene glycol as a regular liquid has been examined for the enhancement of heat transfer. A suitable transformation is used to renovate the leading PDEs into dissimilar ODEs. These equations were solved numerically by bvp4c in MATLAB. Multiple solutions have obtained a precise value of the suction constraint. Thus, the impacts of several governing parameters on the fluid's quantity have been analyzed carefully.

## 2. Mathematical Formulation

Let us consider the 2D MHD movement of a fluid over a shrinking sheet, which is taken to be non-linear, involving  $\text{MoS}_2\text{-SiO}_2$  hybrid nanofluids in ethylene glycol (Carreau liquid) with a boundary condition that is convective in nature. The coordinates of the  $x$ -axis and  $y$ -axis are taken along the path of the movement of the flow and are normal to the shrinking sheet, respectively, as shown in Figure 1. In addition, the hybrid nanoparticles ( $\text{MoS}_2\text{-SiO}_2$ ) in the ethylene glycol are determined to be plasma [28] and non-Newtonian due to the nature of shear thinning [29]. An external magnetic field (variable)  $B(x) = x^{(m-1)/2}B_0$  is oriented in the direction where the fluid is lying, and this magnetic field is almost insignificant when using a small  $R_m$  (magnetic Reynolds number). The variable shrinking velocity is  $u_w = cx^m$ , where  $c > 0$  and  $m > 0$  are constants. The leading PDEs are

$$\frac{\partial u}{\partial x} + \frac{\partial v}{\partial y} = 0 \quad (1)$$

$$u \frac{\partial u}{\partial x} + v \frac{\partial v}{\partial y} = v_{hbnf} \frac{\partial}{\partial y} \left[ \left\{ 1 + \Gamma^2 \left( \frac{\partial u}{\partial y} \right)^2 \right\}^{\frac{n-1}{2}} \frac{\partial u}{\partial y} \right] - \frac{\sigma_{hbnf} B^2}{\rho_{hbnf}} u \quad (2)$$

$$u \frac{\partial T}{\partial x} + v \frac{\partial T}{\partial y} = -\frac{1}{(\rho c_p)_{hbnf}} \frac{\partial q}{\partial y} + \frac{k_{hbnf}}{(\rho c_p)_{hbnf}} \frac{\partial^2 T}{\partial y^2} + \frac{\sigma_{hbnf} B^2}{(\rho c_p)_{hbnf}} (u)^2 + \frac{\mu_{hbnf}}{(\rho c_p)_{hbnf}} \left( \frac{\partial u}{\partial y} \right)^2 \left[ 1 + \Gamma^2 \left( \frac{\partial u}{\partial y} \right)^2 \right]^{\frac{n-1}{2}}, \tag{3}$$

The subjected suitable conditions at the boundary consist of the shrinking velocity, the porous boundary, and the convective temperature condition at the surface, while at the free surface, the temperature and velocity trend toward zero; these conditions are mathematically written as

$$u = -u_w(x), \quad v = -V_w, \quad -k_{hbnf} \frac{\partial T}{\partial y} = h_f (T_f - T) \text{ at } y = 0, T \rightarrow T_\infty, u \rightarrow 0 \text{ as } y \rightarrow \infty. \tag{4}$$

where  $(u, v)$  denotes the constituents of the field velocity in the  $x$ - and  $y$ -axis directions, respectively,  $\nu$ ,  $\rho$ ,  $k$ , and  $\Gamma$  stand for the kinematic viscosity of the fluid, the density, the thermal conductivity, and the relaxation time constant, respectively,  $c_p$ ,  $\sigma$ ,  $n$ ,  $T$ , and  $T_\infty$  denotes the heat (which is specific), the electrical conductivity of the liquid, the power law index, the temperature, and the ambient temperature, respectively. It is important to note that Equation (2) can be reduced to a Newtonian liquid by taking  $n = 1$ . In addition, the value of  $n$  varies as  $0 < n < 1$ , with  $(n < 1 \ \& \ n > 1)$  communicating the behavior of shear thickening and shear thinning fluids.

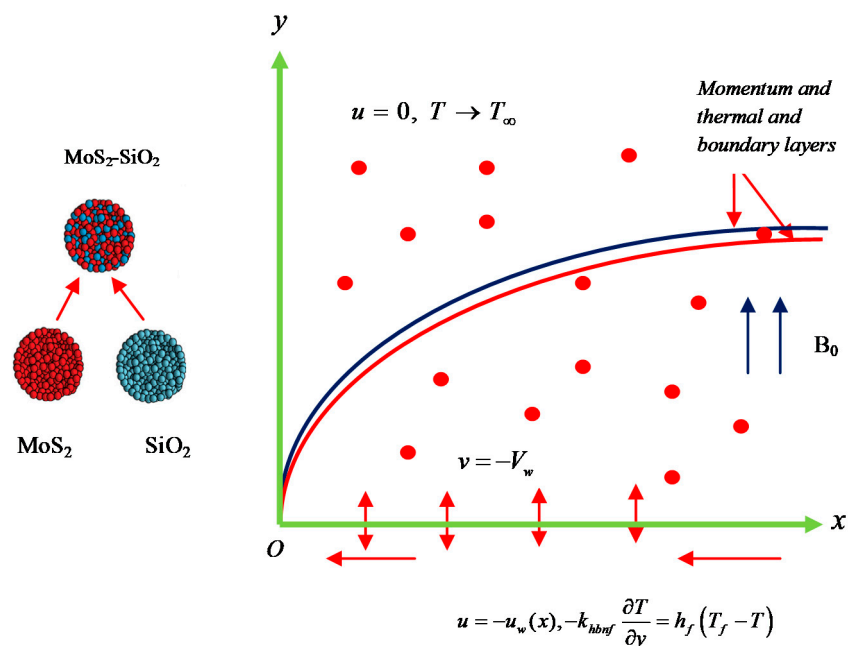


Figure 1. Physical diagram of the problem.

*Thermo-Physical Properties of the Hybrid Nanoliquid*

The mixture of a hybrid nanofluid involving MoS<sub>2</sub> ( $\phi_1$ ) and SiO<sub>2</sub> ( $\phi_2$ ) nanoparticles in water, which is considered a regular fluid. In addition, the nanoparticle volume fractions of SiO<sub>2</sub> have been set to 1%, and those of MoS<sub>2</sub> fluctuate from 1% to 5%. Following the article of Xie et al. [30], the volume fraction of the hybrid nanoliquid is suggested to be

$$\phi_{hmf} = \frac{V_{MoS_2} + V_{SiO_2}}{V_{Total}} = \phi_1 + \phi_2.$$

Moreover, Table 1 is set to explain the thermophysical attributes of the hybrid nanoliquid. In Table 1,  $\rho_f$ ,  $\rho_{s1}$ , and  $\rho_{s2}$  denote the liquid density and solid nanomaterials of MoS<sub>2</sub> and the solid

nanomaterials of SiO<sub>2</sub>;  $(\rho c_p)_{hmbf}$  is the specific heat of the hybrid nanoliquid, while  $(\rho c_p)_f$ ,  $(\rho c_p)_{s_1}$ , and  $(\rho c_p)_{s_2}$  are the regular liquid and the solid nanoparticles of MoS<sub>2</sub> and SiO<sub>2</sub>, respectively;  $\mu_{hmbf}$  and  $\mu_f$  are the hybrid nanoliquid viscosity and regular viscosity, respectively,  $k_{hmbf}$  is the thermal conductivity of the hybrid nanoliquid, and  $k_f$ ,  $k_{s_1}$ , and  $k_{s_2}$  are the thermal conductivity of the regular liquid and the nanoparticles of MoS<sub>2</sub> and SiO<sub>2</sub>, respectively;  $\sigma_{hmbf}$  is the electrical conductivity of the hybrid nanoliquid, and  $\sigma_f$ ,  $\sigma_{s_1}$ ,  $\sigma_{s_2}$ , are the electrical conductivity of the regular liquid and the nanoparticles of MoS<sub>2</sub> and SiO<sub>2</sub>, respectively.

**Table 1.** The thermophysical attributes of the hybrid nanofluid.

Properties	Hybrid Nanofluid
Density	$\rho_{hbnf} = [(1 - \phi_2)\{(1 - \phi_1)\rho_f + \phi_1\rho_{s_1}\} + \phi_2\rho_{s_2}]$
Viscosity	$\frac{\mu_{hbnf}}{\mu_f} = \frac{1}{(1-\phi_1)^{2.5}(1-\phi_2)^{2.5}}$
Electrical conductivity	$\sigma_{hbnf} = \sigma_{bf} \left[ \frac{\sigma_{s_2}(1+2\phi_2)+2\sigma_{bf}(1-\phi_2)}{\sigma_{s_2}(1-\phi_2)+\sigma_{bf}(2+\phi_2)} \right]$ with $\sigma_{bf} = \sigma_f \left[ \frac{\sigma_{s_1}(1+2\phi_1)+2\sigma_f(1-\phi_1)}{\sigma_{s_1}(1-\phi_1)+\sigma_f(2+\phi_1)} \right]$
Thermal conductivity	$\frac{k_{hbnf}}{k_{nf}} = \frac{k_{s_2}+2k_{nf}-2\phi_2(k_{nf}-k_{s_2})}{k_{s_2}+2k_{nf}+\phi_2(k_{nf}-k_{s_2})}$ with $k_{nf} = \frac{k_{s_1}+2k_f-2\phi_1(k_f-k_{s_1})}{k_{s_1}+2k_f+\phi_1(k_f-k_{s_1})} \times k_f$
Heat capacity	$(\rho c_p)_{hmbf} = \left( (1 - \phi_2) \left[ (1 - \phi_1) + \phi_1 \frac{(\rho c_p)_{s_1}}{(\rho c_p)_f} \right] + \phi_2 \frac{(\rho c_p)_{s_2}}{(\rho c_p)_f} \right)$

Following Masood et al. [21] and Mushtaq et al. [31], the heat flux radiative  $q_r$  is expressed as follows:

$$q_r = -\frac{\partial T^4}{\partial y} \frac{4\sigma^*}{3k^*} = -\frac{16\sigma^*}{3k^*} T^3 \frac{\partial T}{\partial y} \tag{5}$$

In the above equation,  $\sigma^*$  and  $k^*$  stand for the Stefan–Boltzmann constant and the coefficient of mean absorption, respectively. Utilizing Equation (5), Equation. (3) can be transmuted as

$$u \frac{\partial T}{\partial x} + v \frac{\partial T}{\partial y} = \frac{\partial}{\partial y} \left[ \frac{\partial T}{\partial y} \left( \frac{k}{\rho c_p} + \frac{16\sigma^* T^3}{3(\rho c_p)k^*} \right) \right]. \tag{6}$$

Introducing the following transformations, we get

$$\psi(x, y) = x^{(m+1)/2} f(\eta) \sqrt{\frac{2cv}{m+1}}, \quad \eta = yx^{(m-1)/2} \sqrt{\frac{c(m+1)}{2v}}, \quad \theta(\eta) = \frac{T - T_\infty}{T_f - T_\infty}. \tag{7a}$$

Here,  $\psi$  represents the (function) called the “Stream Function”, from which we acquire

$$T = T_\infty [1 + (\theta_w - 1)\theta] \tag{7b}$$

in which  $\theta_w > 1$ , where  $\theta_w$  is the existence of the temperature ratio parameter.

Using (7a) and (7b), the nonlinear PDEs (2) and (6) are simplified into the subsequent nonlinear ODEs

$$\frac{\{1 + nWe^2(f'')^2\} \{1 + We^2(f'')^2\}^{\frac{n-3}{2}} f'''}{\Lambda_1} + \Lambda_2 \left\{ f f'' - \left( \frac{2m}{m+1} \right) (f')^2 \right\} - M^2 \Lambda_3 f' = 0, \tag{8}$$

$$\theta'' \left[ \Lambda_4 + \frac{4}{3} R_d (\theta(\theta_w - 1) + 1)^3 \right] + Pr \Lambda_5 f \theta' + 4R_d (\theta_w - 1) (\theta(\theta_w - 1) + 1)^2 (\theta')^2 + \frac{PrEc(f'')^2}{\Lambda_1} \left\{ (1 + We^2(f'')^2)^{\frac{n-1}{2}} \right\} + M^2 PrEc \Lambda_3 (f')^2 = 0 \tag{9}$$

The converted border conditions are

$$\left. \begin{aligned} f(0) = S, \quad \theta'(0) = -\gamma[1 - \theta(0)], \quad f'(0) = -1, \\ f'(\infty) \rightarrow 0, \quad \theta(\infty) \rightarrow 0, \end{aligned} \right\} \tag{10}$$

in which

$$\begin{aligned} \Lambda_1 &= (1 - \phi_1)^{2.5}(1 - \phi_2)^{2.5}, \\ \Lambda_2 &= \left( (1 - \phi_2) \left\{ (1 - \phi_1) + \phi_1 \frac{\rho_{s1}}{\rho_f} \right\} + \phi_2 \frac{\rho_{s2}}{\rho_f} \right), \\ \Lambda_3 &= \left( \frac{\sigma_{s2}(1+2\phi_2)+2\sigma_f \left\{ \frac{\sigma_{s1}(1+2\phi_1)+2\sigma_f(1-\phi_1)}{\sigma_{s1}(1-\phi_1)+\sigma_f(2+\phi_1)} \right\} (1-\phi_2)}{\sigma_{s2}(1-\phi_2)+\sigma_f \left\{ \frac{\sigma_{s1}(1+2\phi_1)+2\sigma_f(1-\phi_1)}{\sigma_{s1}(1-\phi_1)+\sigma_f(2+\phi_1)} \right\} (2+\phi_2)} \right) \left( \frac{\sigma_{s1}(1+2\phi_1)+2\sigma_f(1-\phi_1)}{\sigma_{s1}(1-\phi_1)+\sigma_f(2+\phi_1)} \right), \\ \Lambda_4 &= \left[ \left( \frac{k_{s2}+2k_{nf}-2\phi_2(k_{nf}-k_{s2})}{k_{s2}+2k_{nf}+\phi_2(k_{nf}-k_{s2})} \right) \left( \frac{(k_{s1}+2k_f)-2\phi_1(k_f-k_{s1})}{(k_{s1}+2k_f)+\phi_1(k_f-k_{s1})} \right) \right], \\ \Lambda_5 &= \left( (1 - \phi_2) \left[ (1 - \phi_1) + \phi_1 \frac{(\rho_{cp})_{s1}}{(\rho_{cp})_f} \right] + \phi_2 \frac{(\rho_{cp})_{s2}}{(\rho_{cp})_f} \right). \end{aligned}$$

The aforementioned equations (prime) exhibit the derivatives through  $\eta$ . The local Weissenberg number, the magnetic parameters, the convective parameters, the radiation parameters, the Prandtl number, and the suction parameter are well-defined as

$$\begin{aligned} We^2 &= \frac{c^3(m+1)\Gamma^2 x^{3m-1}}{2\nu}, \quad M^2 = \frac{2\sigma_f B_0^2}{(m+1)c\rho_f}, \quad \gamma = \frac{h_f \sqrt{2\nu/c(m+1)} x^{\frac{1-m}{2}}}{k}, \\ Pr &= \frac{\nu}{\alpha_f}, \quad Rd = \frac{4\sigma^* T_\infty^3}{kk^*}, \quad Ec = \frac{c^2 x^{2m}}{(c_p)_f (\theta_w - 1) T_\infty}, \quad S = V_w x^{\frac{1-m}{2}} \sqrt{2/c\nu(m+1)} > 0 \end{aligned}$$

The physical curiosity quantities are the skin and Nusselt number, which are classified as

$$C_f = \frac{\mu_{hbnf}}{\rho u_w^2} \left( \frac{\partial u}{\partial y} \left[ 1 + \Gamma^2 \left( \frac{\partial u}{\partial y} \right)^2 \right]^{\frac{n-1}{2}} \right)_{y=0}, \quad Nu_x = -\frac{x}{k_f(T_f - T_\infty)} \left[ -k_{hbnf} \left( \frac{\partial T}{\partial y} \right)_w + (q_r)_w \right]. \tag{11}$$

That is,

$$\begin{aligned} C_f Re_x^{1/2} &= \frac{[1 + We^2 (f''(0))^2]^{\frac{n-1}{2}} \sqrt{\frac{m+1}{2}} f''(0)}{(1-\phi_1)^{2.5}(1-\phi_2)^{2.5}}, \\ Nu_x Re_x^{-1/2} &= \frac{-k_{hbnf} \sqrt{\frac{m+1}{2}} \theta'(0) \left[ 1 + \frac{4}{3Rd} \{1 + (\theta_w - 1)\theta(0)\}^3 \right]}{k_f}. \end{aligned} \tag{12}$$

where  $Re_x = cx^{m+1}/\nu$  shows the Reynolds number.

### 3. Stability Analysis of the Solution

When we perform the stability analysis, it is done with the primary objective to obtain the result of the aforementioned problem to quantify and qualify the physical realization of its first branches. This process is also done for the second solution, which is not physically realizable. The unsteady equation that uses a specific order to determine the physical significance of these branches is given as

$$\frac{\partial u}{\partial x} + \frac{\partial v}{\partial y} = 0 \tag{13}$$

$$\begin{aligned} \frac{\partial u}{\partial t} + u \frac{\partial u}{\partial x} + v \frac{\partial v}{\partial y} &= \nu_{hbnf} \frac{\partial^2 u}{\partial y^2} \left[ 1 + \Gamma^2 \left( \frac{\partial u}{\partial y} \right)^2 \right]^{\frac{n-1}{2}} - \frac{\sigma_{hbnf} B_0^2}{\rho_{hbnf}} u \\ &+ \nu_{hbnf} \Gamma^2 (n-1) \frac{\partial^2 u}{\partial y^2} \left( \frac{\partial u}{\partial y} \right)^2 \left[ \Gamma^2 \left( \frac{\partial u}{\partial y} \right)^2 + 1 \right]^{\frac{n-3}{2}} \end{aligned} \tag{14}$$

$$\frac{\partial T}{\partial t} + u \frac{\partial T}{\partial x} + v \frac{\partial T}{\partial y} = -\frac{1}{(\rho c_p)_{hbnf}} \frac{\partial q_r}{\partial y} + \frac{k_{hbnf}}{(\rho c_p)_{hbnf}} \frac{\partial^2 T}{\partial y^2} + \frac{\sigma_{hbnf} B^2}{(\rho c_p)_{hbnf}} (u)^2 + \frac{\mu_{hbnf}}{(\rho c_p)_{hbnf}} \left(\frac{\partial u}{\partial y}\right)^2 \left[1 + \Gamma^2 \left(\frac{\partial u}{\partial y}\right)^2\right]^{\frac{n-1}{2}}, \tag{15}$$

Using the aforementioned model of stability, we declare the fresh time variable that is dimensionless ( $\tau$ ). For this stability model, the similarity transformation now becomes

$$u = cx^m \frac{\partial f(\eta, t)}{\partial \eta}, \quad v = -x^{(m-1)/2} \sqrt{\frac{cv(m+1)}{2}} f(\eta, t) - \frac{yc(m-1)}{2} x^{m-1} \frac{\partial f(\eta, t)}{\partial \eta}, \tag{16}$$

$$\eta = x^{(m-1)/2} y \sqrt{\frac{c(m+1)}{2v}}, \quad \tau = cx^{m-1} t, \quad \theta(\eta, t) = \frac{T-T_\infty}{T_f-T_\infty}.$$

By inserting Equation (16) into Equations (14) and (15), we get

$$\frac{\frac{\partial^3 f}{\partial \eta^3} \left(1+nWe^2 \left(\frac{\partial^2 f}{\partial \eta^2}\right)^2\right)^{\frac{n-3}{2}} \left\{1+nWe^2 \left(\frac{\partial^2 f}{\partial \eta^2}\right)^2\right\}}{\Lambda_1} + \Lambda_2 \left\{f \frac{\partial^2 f}{\partial \eta^2} - \left(\frac{2m}{m+1}\right) \left(\frac{\partial f}{\partial \eta}\right)^2\right\} - \Lambda_2 \left(\frac{2}{m+1}\right) \left\{(m-1)\tau \frac{\partial f}{\partial \eta} \frac{\partial^2 f}{\partial \eta \partial \tau} + \frac{\partial^2 f}{\partial \eta \partial \tau}\right\} - M^2 \Lambda_3 \frac{\partial f}{\partial \eta} = 0, \tag{17}$$

$$\frac{\partial^2 \theta}{\partial \eta^2} \left[\Lambda_4 + \frac{4}{3} R_d (\theta(\theta_w - 1) + 1)^3\right] + \Lambda_5 \text{Pr} f(\eta, t) \frac{\partial \theta}{\partial \eta} + 4R_d (\theta_w - 1) (\theta(\theta_w - 1) + 1)^2 \left(\frac{\partial \theta}{\partial \eta}\right)^2 + \frac{\text{PrEc}}{\Lambda_1} \left(\frac{\partial^2 f}{\partial \eta^2}\right)^2 \left\{\left(1 + We^2 \left(\frac{\partial^2 f}{\partial \eta^2}\right)^2\right)^{\frac{n-1}{2}}\right\} + M^2 \text{PrEc} \Lambda_3 \left(\frac{\partial f}{\partial \eta}\right)^2 - \left(\frac{2\text{Pr}}{m+1}\right) \Lambda_5 \left\{\frac{\partial \theta}{\partial \tau} + (m-1)\tau \frac{\partial f}{\partial \eta} \frac{\partial \theta}{\partial \tau}\right\} = 0, \tag{18}$$

and the subjected conditions are

$$f(0, \tau) = S, \quad \frac{\partial \theta(0, \tau)}{\partial \eta} = -\gamma(1 - \theta(0, \tau)), \quad \frac{\partial f(0, \tau)}{\partial \eta} = -1, \quad \text{at } \eta = 0$$

$$\frac{\partial f(\eta, \tau)}{\partial \eta} \rightarrow 0, \quad \theta(\eta, \tau) \rightarrow 0 \text{ as } \eta \rightarrow \infty \tag{19}$$

To check the steady flow solution’s stability, let us use  $f(\eta) = f_0(\eta)$  and  $\theta(\eta) = \theta_0(\eta)$ , which satisfy the BVP (2)–(5). Then, we implement the following (Merkin [32], Weidman et al. [33], and Zaib et al. [34]).

Let

$$f(\eta, \tau) = e^{-\beta\tau} F(\eta, \tau) + f_0(\eta)$$

$$\theta(\eta, \tau) = e^{-\beta\tau} G(\eta, \tau) + \theta_0(\eta) \tag{20}$$

where “ $\beta$ ” is a value with an unknown (the growth and decay distribution) eigenvalue, and  $F(\eta, \tau)$  &  $G(\eta, \tau)$  are too small to allow  $f_0(\eta)$  and  $\theta_0(\eta)$ , respectively.

Then, inserting Equation (20) into Equations (17)–(19), we infer the subsequent equations:

$$\frac{\left(e^{-\beta\tau} \frac{\partial^3 F}{\partial \eta^3} + \frac{\partial^3 f_0}{\partial \eta^3}\right) \left\{1+nWe^2 \left(e^{-\beta\tau} \frac{\partial^2 F}{\partial \eta^2} + \frac{\partial^2 f_0}{\partial \eta^2}\right)^2\right\} \left(1+We^2 \left(e^{-\beta\tau} \frac{\partial^2 F}{\partial \eta^2} + \frac{\partial^2 f_0}{\partial \eta^2}\right)^2\right)^{\frac{n-3}{2}}}{\Lambda_1} + \Lambda_2 \left\{\left(e^{-\beta\tau} F + f_0\right) \left(e^{-\beta\tau} \frac{\partial^2 F}{\partial \eta^2} + \frac{\partial^2 f_0}{\partial \eta^2}\right) - \left(\frac{2m}{m+1}\right) \left(e^{-\beta\tau} \frac{\partial F}{\partial \eta} + \frac{\partial f_0}{\partial \eta}\right)^2\right\} - \Lambda_2 \left(\frac{2}{m+1}\right) \left\{(m-1)\tau \left(e^{-\beta\tau} \frac{\partial F}{\partial \eta} + \frac{\partial f_0}{\partial \eta}\right) \left(-\beta e^{-\beta\tau} \frac{\partial F}{\partial \eta} + e^{-\beta\tau} \frac{\partial^2 F}{\partial \eta \partial \tau}\right) + \left(-\beta e^{-\beta\tau} \frac{\partial F}{\partial \eta} + e^{-\beta\tau} \frac{\partial^2 F}{\partial \eta \partial \tau}\right)\right\} - M^2 \Lambda_3 \left(e^{-\beta\tau} \frac{\partial F}{\partial \eta} + \frac{\partial f_0}{\partial \eta}\right) = 0, \tag{21}$$

$$\begin{aligned} & \left( \frac{\partial^2 \theta_0}{\partial \eta^2} + e^{-\beta \tau} \frac{\partial^2 G}{\partial \eta^2} \right) \left[ \Lambda_4 + \frac{4}{3} R_d \left( (\theta_0 + e^{-\beta \tau} G)(\theta_w - 1) + 1 \right)^3 \right] + \\ & \Lambda_4 \Pr \left( e^{-\beta \tau} F + f_0 \right) \left( \frac{\partial \theta_0}{\partial \eta} + e^{-\beta \tau} \frac{\partial G}{\partial \eta} \right) + 4 R_d (\theta_w - 1) \left( (\theta_w - 1)(\theta_0 + e^{-\beta \tau} G) + 1 \right)^2 \left( \frac{\partial \theta_0}{\partial \eta} + e^{-\beta \tau} \frac{\partial G}{\partial \eta} \right)^2 \\ & \frac{\Pr Ec}{\Lambda_1} \left( e^{-\beta \tau} \frac{\partial^2 F}{\partial \eta^2} + \frac{\partial^2 f_0}{\partial \eta^2} \right)^2 \left\{ \left( 1 + We^2 \left( e^{-\beta \tau} \frac{\partial^2 F}{\partial \eta^2} + \frac{\partial^2 f_0}{\partial \eta^2} \right)^2 \right)^{\frac{n-1}{2}} \right\} + M^2 \Pr Ec \Lambda_3 \left( e^{-\beta \tau} \frac{\partial F}{\partial \eta} + \frac{\partial f_0}{\partial \eta} \right)^2 \\ & - \left( \frac{2 \Pr}{m+1} \right) \Lambda_5 \left\{ e^{-\beta \tau} \frac{\partial G}{\partial \tau} - \beta e^{-\beta \tau} G + (m-1) \tau \left( e^{-\beta \tau} \frac{\partial G}{\partial \tau} - \beta e^{-\beta \tau} G \right) \left( e^{-\beta \tau} \frac{\partial F}{\partial \eta} + \frac{\partial f_0}{\partial \eta} \right) \right\} = 0, \end{aligned} \tag{22}$$

with the conditions given as

$$\begin{aligned} F(0, \tau) = 0, \frac{\partial G(0, \tau)}{\partial \eta} = \gamma G(0, \tau), \frac{\partial F(0, \tau)}{\partial \eta} = 0, \text{ at } \eta = 0 \\ \frac{\partial F(\eta, \tau)}{\partial \eta} \rightarrow 0, G(\eta, \tau) \rightarrow 0 \text{ as } \eta \rightarrow \infty \end{aligned} \tag{23}$$

Then, for  $n = 3$ , we achieve the subsequent linearized problems:

$$\begin{aligned} & \left( \frac{1 + 3We^2 \left( \frac{\partial^2 f_0}{\partial \eta^2} \right)^2}{\Lambda_1} \frac{\partial^3 F}{\partial \eta^3} + 6We^2 \frac{\partial^3 f_0}{\partial \eta^3} \frac{\partial^2 f_0}{\partial \eta^2} \frac{\partial^2 F}{\partial \eta^2} \right) + \Lambda_2 \left\{ \begin{aligned} & f_0 \frac{\partial^2 F}{\partial \eta^2} + F \frac{\partial^2 f_0}{\partial \eta^2} \\ & - \frac{\partial F}{\partial \eta} \left( \frac{4m}{m+1} \right) \frac{\partial f_0}{\partial \eta} \end{aligned} \right\} \\ & + \frac{2\beta}{m+1} \Lambda_2 \frac{\partial F}{\partial \eta} - M^2 \Lambda_3 \frac{\partial F}{\partial \eta} = 0, \end{aligned} \tag{24}$$

$$\begin{aligned} & \frac{\partial^2 G}{\partial \eta^2} \left[ \Lambda_4 + \frac{4}{3} R_d (\theta (\theta_w - 1) + 1)^3 \right] + \Lambda_5 \Pr \left( f_0 \frac{\partial G}{\partial \eta} + F \frac{\partial \theta_0}{\partial \eta} \right) + \\ & \frac{2 \Pr Ec}{\Lambda_1} \frac{\partial^2 F}{\partial \eta^2} \frac{\partial^2 f_0}{\partial \eta^2} \left\{ 1 + 2We^2 \left( \frac{\partial^2 f_0}{\partial \eta^2} \right)^2 \right\} + 8 R_d (\theta_w - 1)^2 (\theta (\theta_w - 1) + 1)^2 G \left( \frac{\partial \theta_0}{\partial \eta} \right)^2 + \\ & 8 R_d (\theta (\theta_w - 1) + 1)^2 \frac{\partial G}{\partial \eta} \frac{\partial \theta_0}{\partial \eta} + M^2 \Pr Ec \Lambda_3 \left( 2 \frac{\partial F}{\partial \eta} \frac{\partial f_0}{\partial \eta} \right) + \left( \frac{2 \Pr}{m+1} \right) \beta G \Lambda_5 = 0, \end{aligned} \tag{25}$$

Following Weidman et al. [33], we investigated a stable solution for the phenomenon of steady flow  $f_0(\eta)$  with a heat transfer solution  $\theta_0(\eta)$  through site  $\tau = 0$ ; therefore,  $F = F_0(\eta)$  and  $G = G_0(\eta)$  in (24) and (25) are used to classify the early increase/deterioration of the result. In this way, we explain the subsequent linear eigenvalue problem:

$$\begin{aligned} & \left( \frac{F_0''' (1 + 3We^2 (f_0'')^2) + 6We^2 f_0''' f_0'' F_0''}{\Lambda_1} \right) + \Lambda_2 \left\{ \begin{aligned} & f_0 F_0'' + F_0 f_0'' - \\ & \left( \frac{4m}{m+1} \right) f_0' F_0' \end{aligned} \right\} \\ & + \frac{2\beta}{m+1} \Lambda_2 F_0' - M^2 \Lambda_3 F_0' = 0, \end{aligned} \tag{26}$$

$$\begin{aligned} & G_0'' \left[ \Lambda_4 + \frac{4}{3} R_d (\theta_0 (\theta_w - 1) + 1)^3 \right] + \Lambda_5 \Pr (f_0 G_0' + F_0 \theta_0') + \\ & \frac{2 \Pr Ec}{\Lambda_1} F_0'' f_0'' \left\{ 1 + 2We^2 (f_0'')^2 \right\} + 8 R_d (\theta_w - 1)^2 (\theta_0 (\theta_w - 1) + 1)^2 G_0 (\theta_0')^2 + \\ & 8 R_d (\theta_0 (\theta_w - 1) + 1)^2 G_0' \theta_0' + M^2 \Pr Ec \Lambda_3 (2 F_0' f_0') + \left( \frac{2 \Pr}{m+1} \right) \beta G_0 \Lambda_5 = 0, \end{aligned} \tag{27}$$

and conditions at the boundary are

$$\begin{aligned} F_0(0) = 0, G_0' = \gamma G_0(0), F_0' = 0, \text{ at } \eta = 0 \\ F_0' \rightarrow 0, G_0 \rightarrow 0 \text{ as } \eta \rightarrow \infty \end{aligned} \tag{28}$$

In this research, we explain the linear eigenvalue system of IVP (26)–(27) with a new boundary condition (28) by relaxing the conditions  $F_0(\eta)$  and  $G_0(\eta)$ . Here, the condition  $G_0 \rightarrow 0$  as  $\eta \rightarrow \infty$  is relaxed, and, for a fixed value of  $\gamma$ , we calculate (26) and (27) along with the fresh boundary condition,  $G_0(0) = 1$ .

#### 4. Results and Discussion

The transmuted system of the non-linear ODEs (8) and (9) through condition (10) were deciphered numerically through the `bvp4c` named via MATLAB for the assorted standards of the pertinent

parameters. For the numerical simulation, we can fix the range of the pertinent parameters throughout the study as  $0 \leq \phi_1 \leq 0.9$ ,  $0 \leq \phi_2 \leq 0.9$ ,  $0 \leq M \leq 0.5$ ,  $0.1 \leq n \leq 3.5$ ,  $0 \leq \gamma \leq 1.5$ ,  $0.1 \leq R_d \leq 3$ ,  $0.1 \leq Ec \leq 2.5$ ,  $0 \leq We \leq 3.5$ , and  $0.1 \leq m \leq 1.5$ . The thermo–physical characteristics of the ethylene glycol and the hybrid (MoS<sub>2</sub>/SiO<sub>2</sub>) nanofluids are shown in Table 2. Moreover, the results in Table 3 are in excellent harmony with the previously published results on a limited case, and excellent agreement has been observed. Here, we found more than one solution (dual solution) throughout the study, where the first solution is represented by the solid green lines, and the second solution is represented by red dashed lines, while the critical point is marked by the small red dot. Figures 2 and 3 show the influences of  $\phi_1$  and  $\phi_2$  on the liquid velocity and the temperature profiles, respectively. These pictures show that the liquid velocity increases in the upper branch solution and declines in the lower branch solution by augmenting  $\phi_1$  and  $\phi_2$ , which ultimately widens the velocity boundary layer thickness. On the other hand, similar behavior is shown in Figure 3, which demonstrates that the temperature distribution, as well as the thermal boundary layer, increases in the first branch solution due to  $\phi_1$  and  $\phi_2$  and decelerates in the second branch solution as we augment the value of the ethylene glycol hybrid nanofluid. Physically, the scattering of the hybrid nanoparticles augments the exchange of thermal energy in the hybrid nanofluid layer, which is bordered on the sheet and the next adjoining hybrid nanofluid layers’ dispersion of nanoparticles. Thus, the present results suggest that the utilization of hybrid nanoparticles can help us to develop better heat distribution in particular heat transfer equipment and can save energy through chemical processes. More generally, the augmentation of the hybrid nanomaterials shows an increment in the thermal conductivity and its temperature profile for the upper branch solution, which declines for the lower branch solution in some range along the  $x$ -axis and then suddenly starts increasing in the second branch solution for the temperature distribution. Due to microscopic instrument, this trend can now be detected and observed. By exercising the ethylene glycol hybrid nanofluid with the base fluid ethylene glycol and making a hybrid mixture, we developed the characteristic features of the thermal suspension. As a result, greater thermal capacity was found due to the mixture of the hybrid nanoparticles.

**Table 2.** The thermophysical properties of the base fluid (ethylene glycol) and the ethylene glycol hybrid nanoparticles [35,36].

Characteristic Properties	Ethylene Glycol	SiO <sub>2</sub>	MoS <sub>2</sub>
$\rho$	1113.5	2650	5060
$c_p$	2430	730	397.746
$k$	0.253	1.5	34.5
$\sigma$	$4.3 \times 10^{-5}$	0.0005	$1 \times 10^{-18}$
Pr	204		

**Table 3.** Comparison of the values of  $-\theta'(0)$  when  $We = S = R_d = 0, m = 1, \gamma = \infty$ .

Pr	Ref. [37]		Present Research	
	First Solution	Second Solution	First Solution	Second Solution
0.7	0.454501	0.377110	0.4539	0.3772
2.0	0.911411	0.881301	0.9114	0.8813
7.0	1.895400	1.880900	1.8954	1.8810

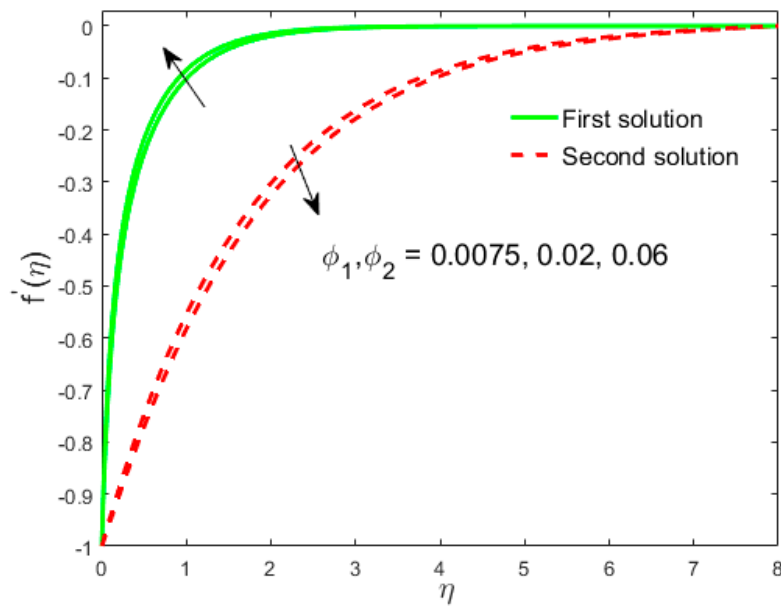


Figure 2. Influence of  $\phi_1, \phi_2$  on  $f'(\eta)$ .

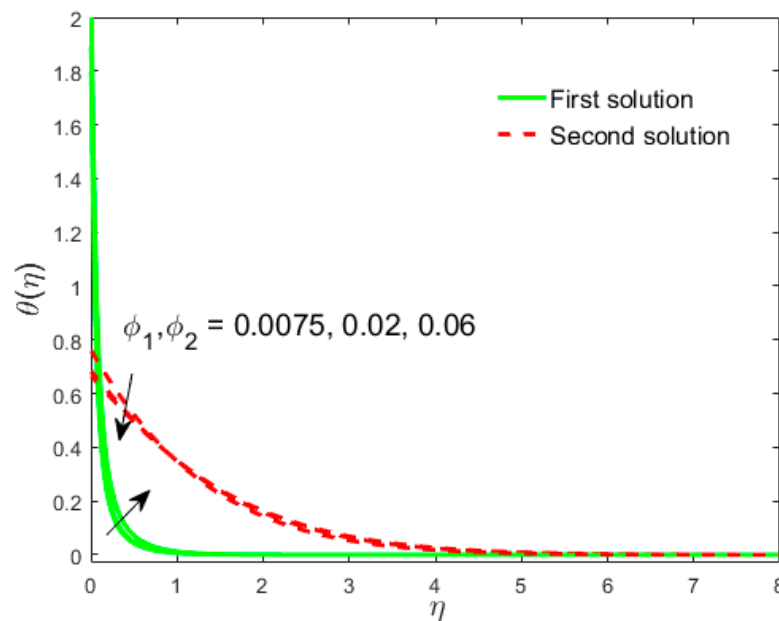


Figure 3. Influence of  $\phi_1, \phi_2$  on  $\theta(\eta)$ .

Figures 4 and 5 exhibit the liquid velocity and temperature profile for numerous choices of  $n$ . Figure 4 demonstrates that the liquid velocity decreases with escalating values of  $n$ , and, as a result, the velocity boundary layer grows thicker and thicker in the first solution, while for the second branch solution, there is an increase in the velocity of the flow. It is also apparent in this plot that the width of the border layer is higher only for the thickening liquid associated with the thinning liquid. Further, the border layer width is thicker for the first solution compared to the second solution. Figure 5 shows that the liquid temperature increases with bigger values of  $n$  in the first solution and decreases in the second solution. Hence, the temperature boundary layer width becomes thicker and thicker for the first solution but becomes thinner in the second solution. Notably, both solutions can placate the boundary conditions asymptotically, thereby validating the numerical outcomes of this problem.

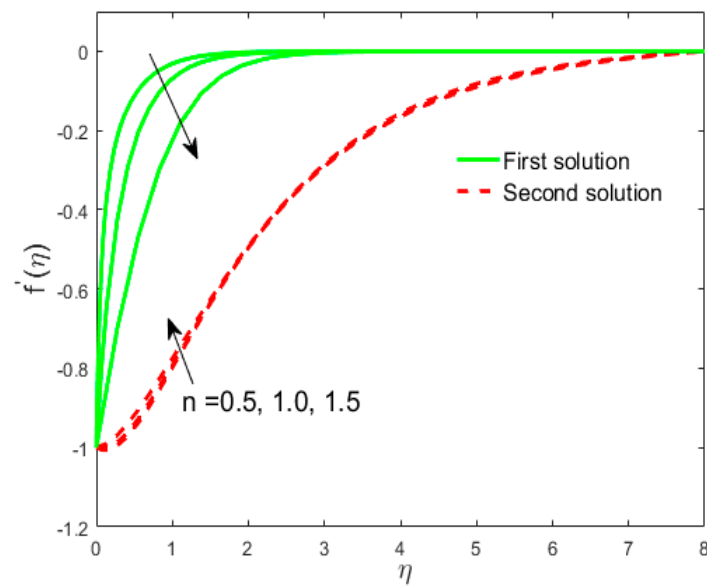


Figure 4. Influence of  $n$  on  $f'(\eta)$ .

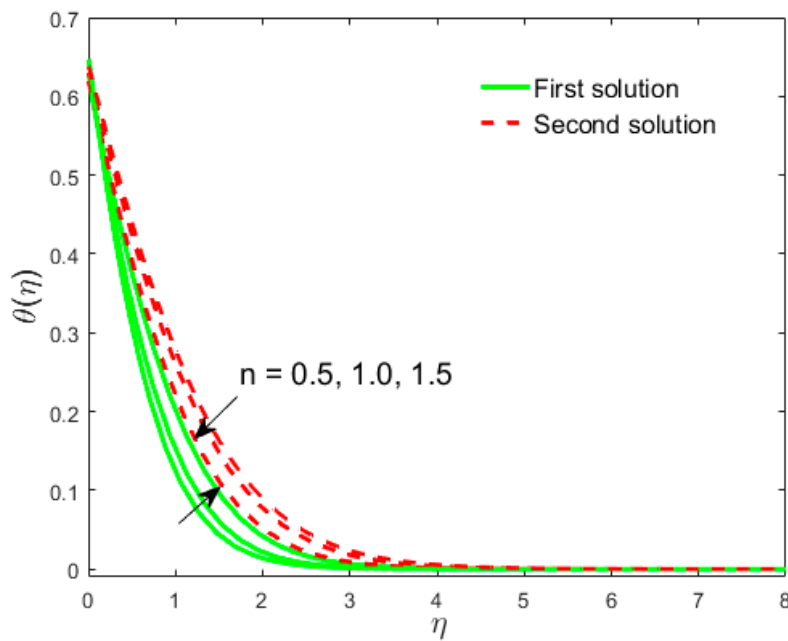


Figure 5. Influence of  $n$  on  $\theta(\eta)$ .

In Figures 6 and 7, the impacts of  $M$  on the velocity distribution and the temperature profile are given for shear thinning and thickening fluids, respectively. Figure 6 shows that the liquid velocity increases in the first solution and decreases in the second solution for both phenomena of liquids. Therefore, the velocity boundary thickness shrinks in the first solution and increases in the second solution for shear thickening and thinning liquids. Physically, magnetic force increases liquid motion inside the boundary layer, as well as of the final expression of Equation (2), which remains positive in the region. Moreover, the crosswise magnetic impact on the electrically leading liquid increases the resistive force identified as a Lorentz force. This Lorentz force has the tendency to speed up liquid motion in the boundary region. This graph also shows that the profiles are more pronounced for the shear thickening liquid in comparison to those for the shear thinning liquid for the first solution. In contrast, Figure 7 indicates that the temperature profiles increase with higher values of  $M$  for the first branch solution because the temperature boundary layer becomes thicker and thicker for shear

thinning liquid, while an opposite tendency is realized for the solution of the second branch. However, for shear thickening fluid, the temperature profiles behave in an opposite manner.

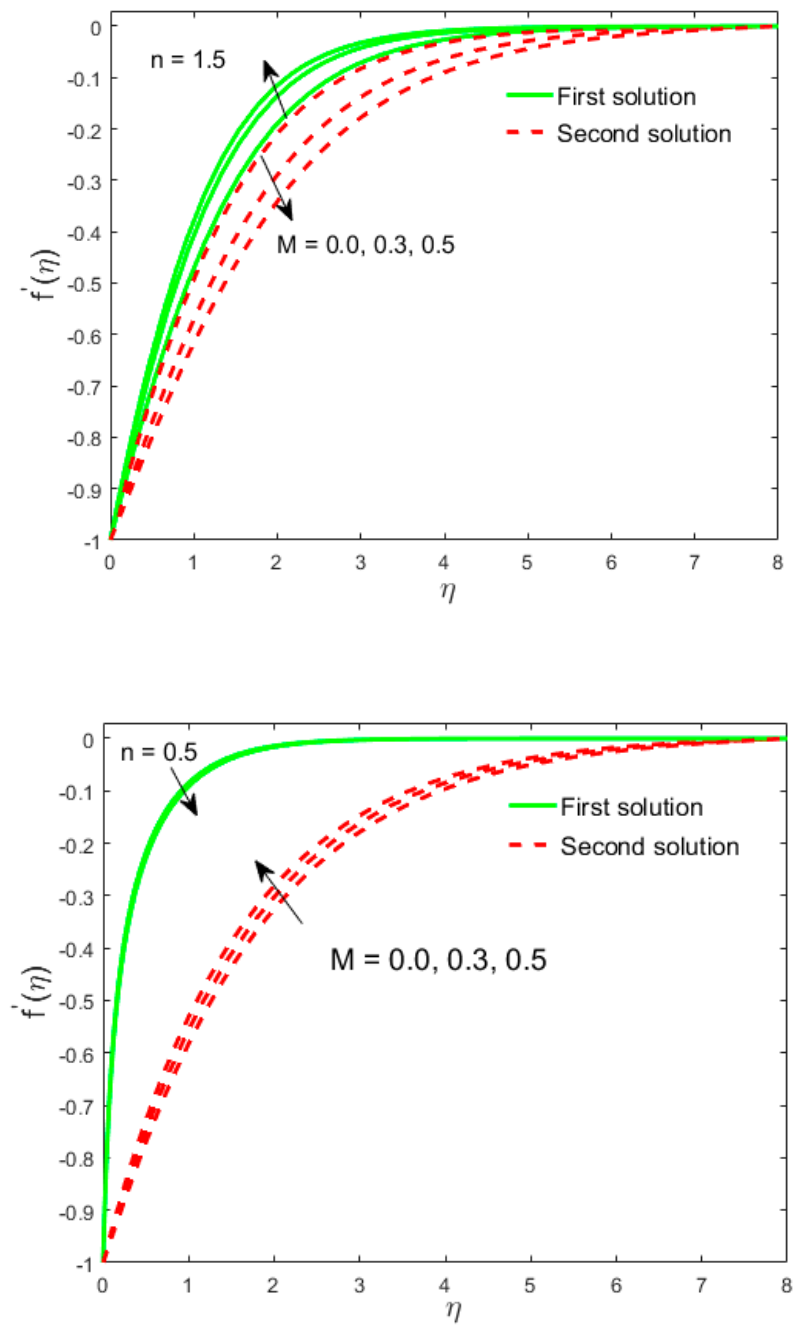


Figure 6. Influence of  $M$  on  $f'(\eta)$ .

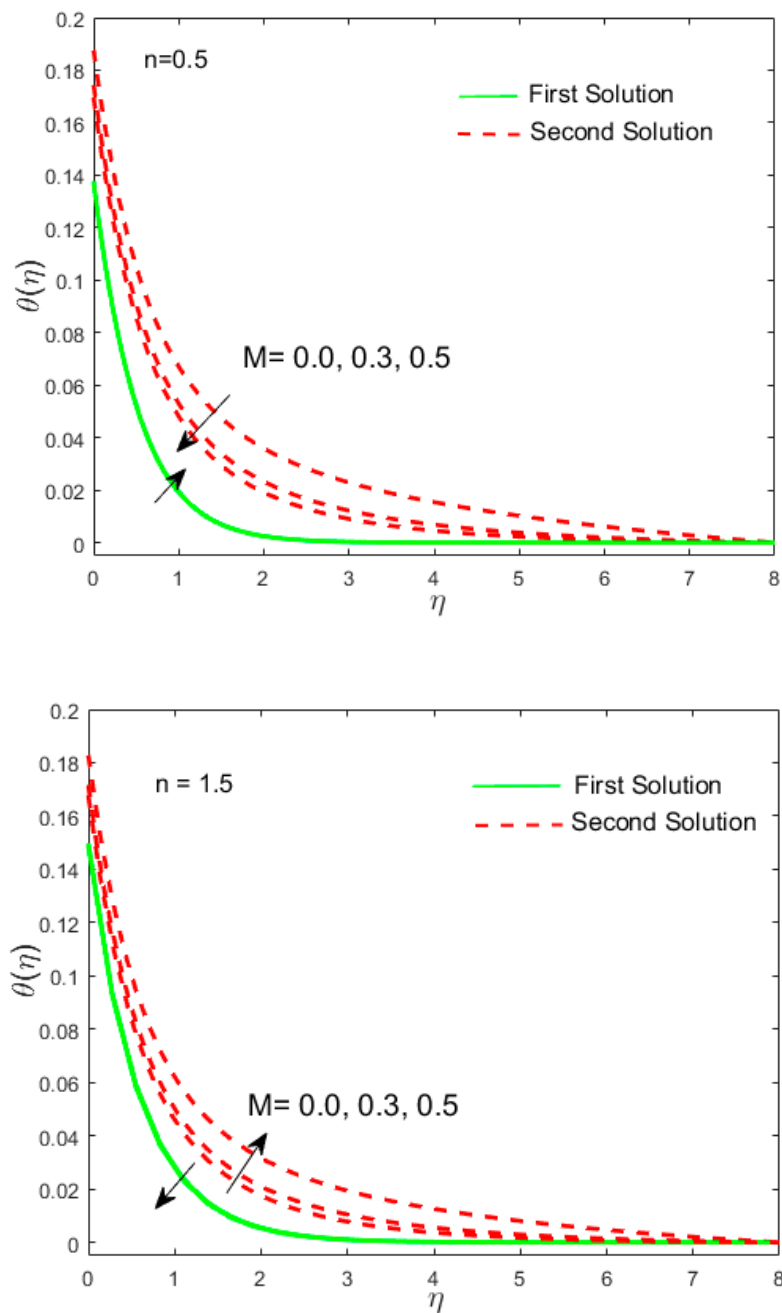


Figure 7. Influence of  $M$  on  $\theta(\eta)$ .

Figures 8 and 9 illustrate the performance of the flow of the liquid and the temperature distribution of several choices of  $We$ . Figure 8 shows that the liquid velocity declines due to the  $We$  in the first solution; therefore, the thickness of the momentum boundary layer increases, whereas, for the second solution, the boundary layer width declines. Also, it is apparent from these plots that the first solution shows greater boundary viscosity than the second solution. The temperature boundary layer thus becomes thicker and thicker with an increase in  $We$  in the first solution and declines in the second solution, as shown in Figure 9. Physically,  $We$  indicates the relation of elastic and viscous forces; it increases the thickness of the hybrid nanofluid, thereby increasing temperature.

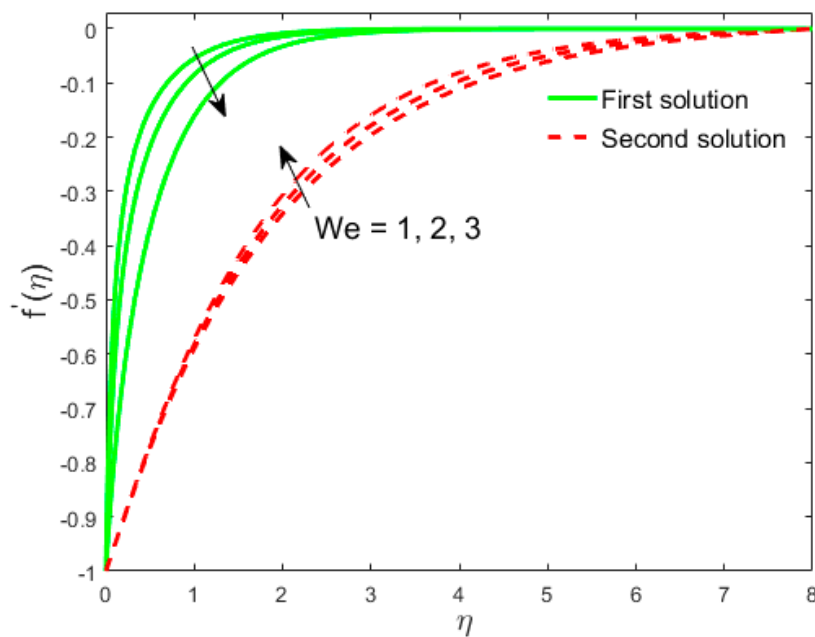


Figure 8. Influence of  $We$  on  $f'(\eta)$ .

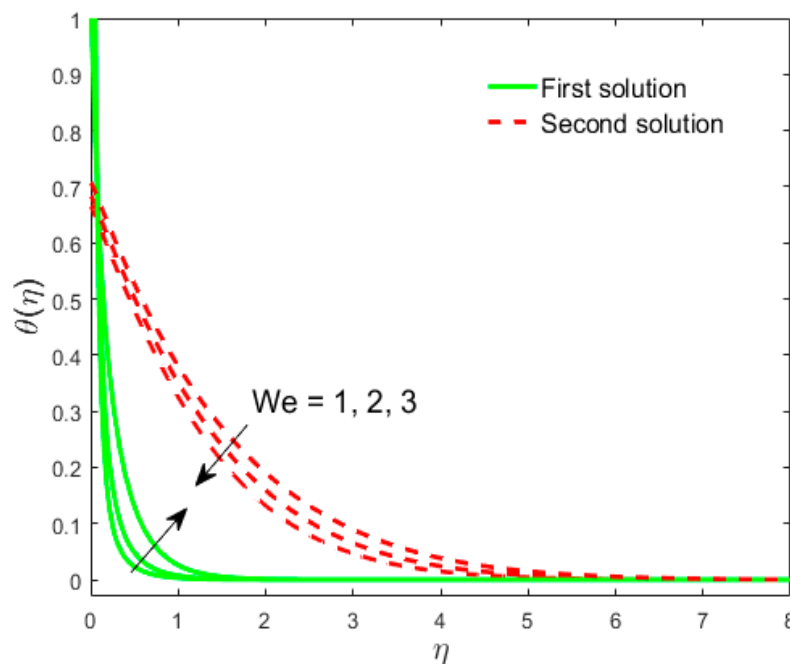


Figure 9. Influence of  $We$  on  $\theta(\eta)$ .

Figure 10 demonstrates that the temperature distribution decreases with higher values of  $R_d$  in the first and second solutions. Consequently, the temperature borderline layer becomes thicker and thicker and then thinner and thinner for the branch of the first solution, as well as for the second branch solution. Physically, the greater values of  $R_d$  suggest the importance of conduction and, consequently, decrease the thickness of the temperature profile layer. Figure 11 depicts the temperature parameter impact  $\theta_w$  on the temperature distribution. It can be perceived from this portrait that an increment in  $\theta_w$  indicates a larger wall temperature compared to the ambient liquid. As a result, the temperature of the liquid increases for both the first and second solutions. Further, the thickness of the temperature boundary layer increases exponentially under increasing values of  $\theta_w$ . The Eckert number was found in a dimensionless form of ODE due to the presence of the viscous dissipation term in the energy

equation, which can use the augmentation in the dissipation heat because of the higher value of the Eckert number. As a result, the temperature of the liquid increases. This fact is depicted by Figure 12, where the Eckert parameter's impact  $Ec$  on the temperature distribution and dual solutions was found. Further, it can be perceived from this portrait that an increment in the  $Ec$  number generates more work done by the force of friction. As a result, the temperature of the liquid increases for both the first and second solutions. Physically, the temperature boundary layer becomes thicker and thicker, increasing the values of the  $Ec$  number. This is done due to an escalation of the internal energy of the liquid, which is defined by the first law of thermodynamics.

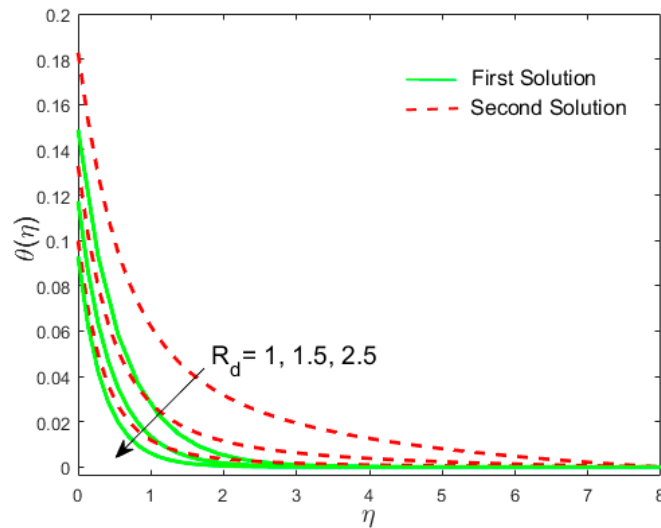


Figure 10. Effect of  $R_d$  on  $\theta(\eta)$ .

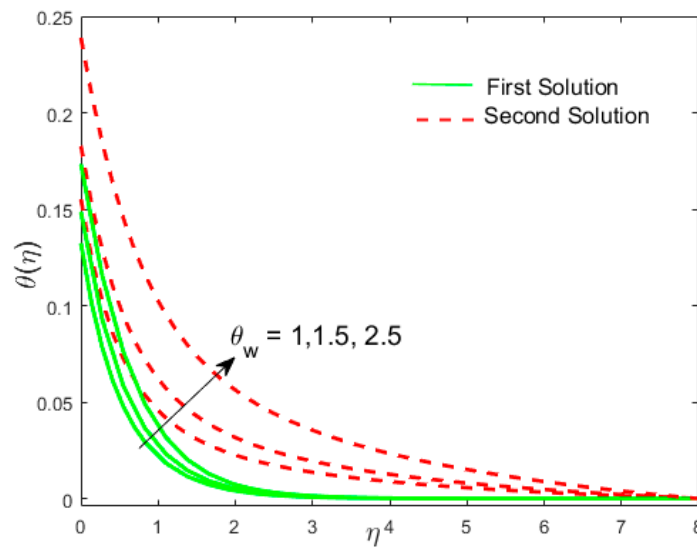


Figure 11. Effect of  $\theta_w$  on  $\theta(\eta)$ .

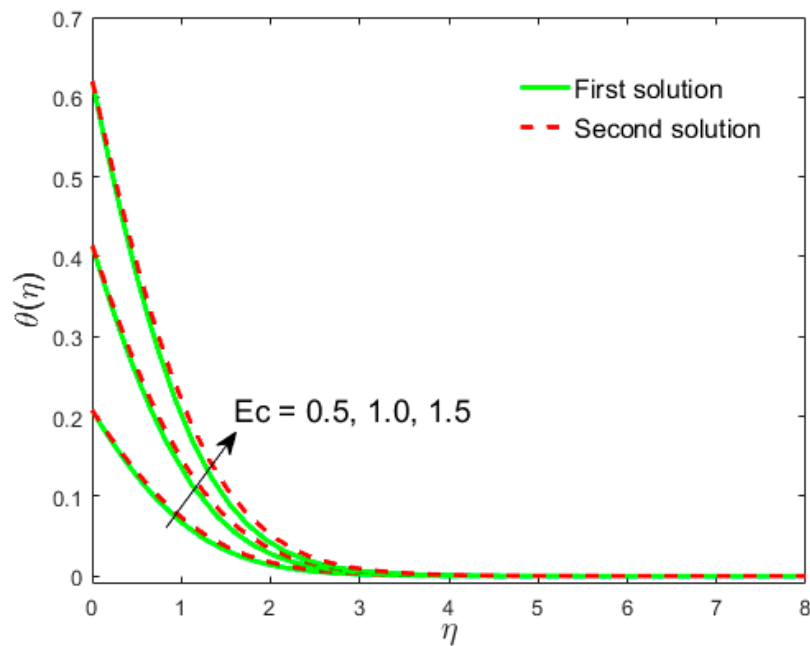


Figure 12. Effect of  $Ec$  on  $\theta(\eta)$ .

Figure 13 shows that the growing values of  $\gamma$  approach tougher convective heating at the surface of the sheet, which increases the temperature slope at the surface for the first and second solutions. This allows the thermal impact to penetrate deeper into the sluggish boundary layer augmented with  $\gamma$ . It is understood that the wall constant temperature  $\theta(0) = 1$  can be recovered by making  $\gamma$  adequately large. In addition,  $\gamma = 0$  communicates the insulated surface case.

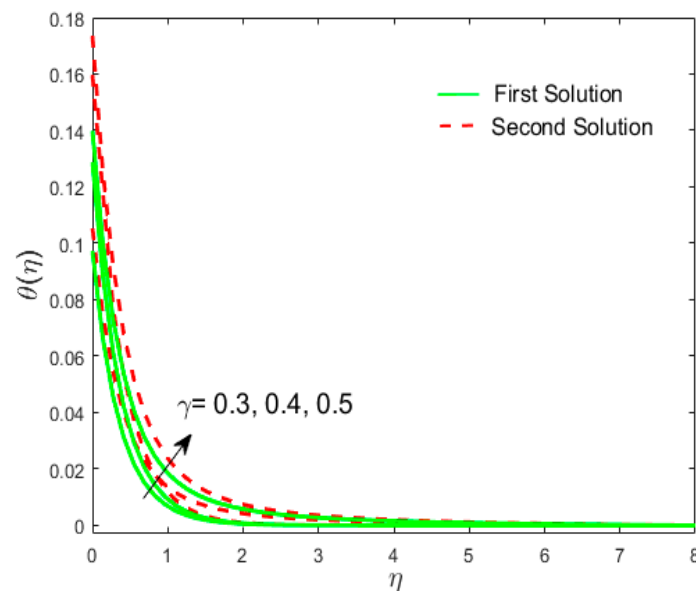


Figure 13. Influence of  $\gamma$  on  $\theta(\eta)$ .

The  $C_{fx}Re_x^{1/2}$  and the local Nusselt number  $Nu_xRe_x^{-1/2}$  versus  $S$  are portrayed in Figures 14 and 15, respectively. Figures 14 and 15 demonstrate that the choices of skin factor and  $Nu_xRe_x^{-1/2}$  decline by mounting  $We$  in the first solution, while in second solution, the values increase. This figure also shows that these  $Nu_xRe_x^{-1/2}$  values always remain positive, which means that the temperature shifts from a warm surface to a cold liquid. Moreover, the multiple non similar results found the critical values of  $S = S_c (< 0)$ , past which no result survives. Calculations showed that the critical values are

1.9699, 2.0700, and 2.2370 for  $We = 1, 2, 3$ , respectively. Thus, the Weissenberg number accelerates the boundary layer separation.

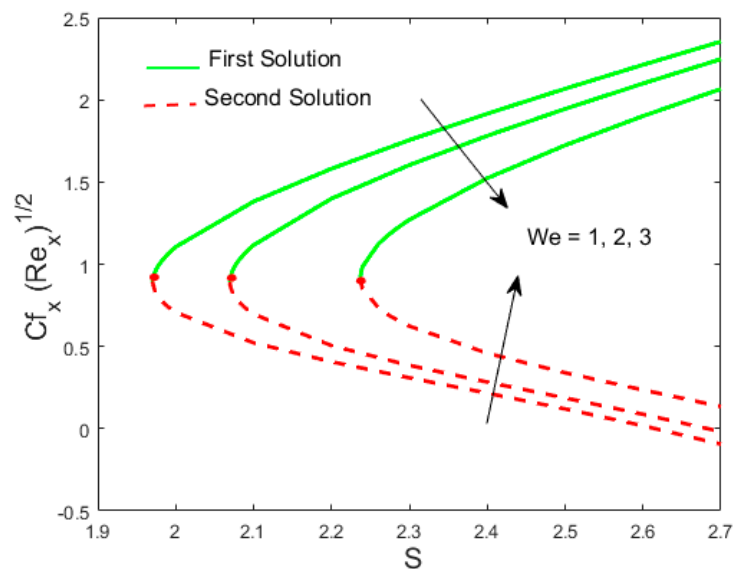


Figure 14. Impact of  $We$  versus  $S$  on  $C_{fx}Re_x^{1/2}$ .

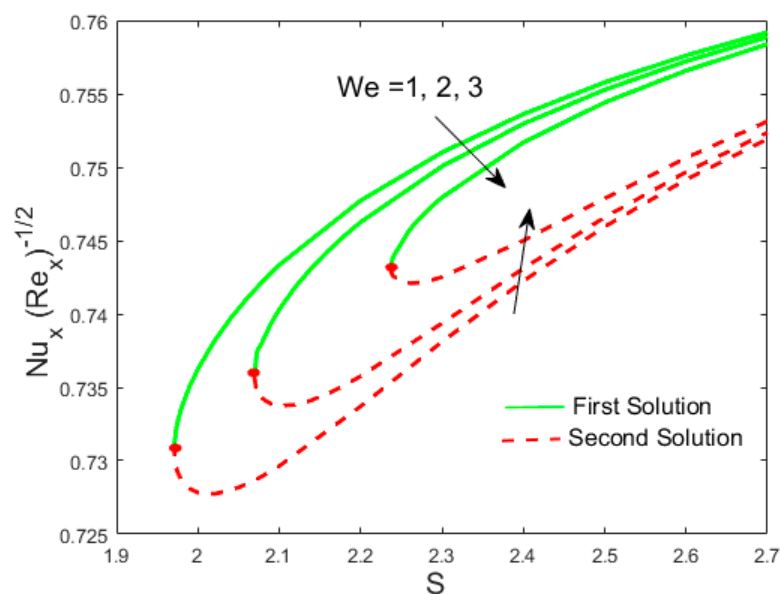


Figure 15. Impact of  $We$  versus  $S$  on Nusselt.

Figures 16 and 17 illustrate the aberration of  $Nu_x Re_x^{-1/2}$  &  $C_{fx} Re_x^{1/2}$  for the distinct choices of  $M$ . Further, we observed that multiple results exist for the variations in parameter  $M$  by keeping all other parameters stable. In these graphs, we observed that an augmentation in  $M$  communicates an important development in the skin factor and Nusselt number for the phenomenon of the first branch solution. In addition, the coefficients of the skin friction and heat transfer of the local rate reduce due to larger magnetic parameters in the second solution. The greatest magnetic constraint developed a drag-like force recognized as a Lorentz force. This force operates as a mediator that opposes the liquid flow and makes progress in the heat transfer rate along with the local skin coefficient. In addition, both graphs show that the size of the center line at the peak of the stationary values (i.e.,  $|S_c|$ ) leans toward augmentation due to its superior determination of the magnetic parameters.

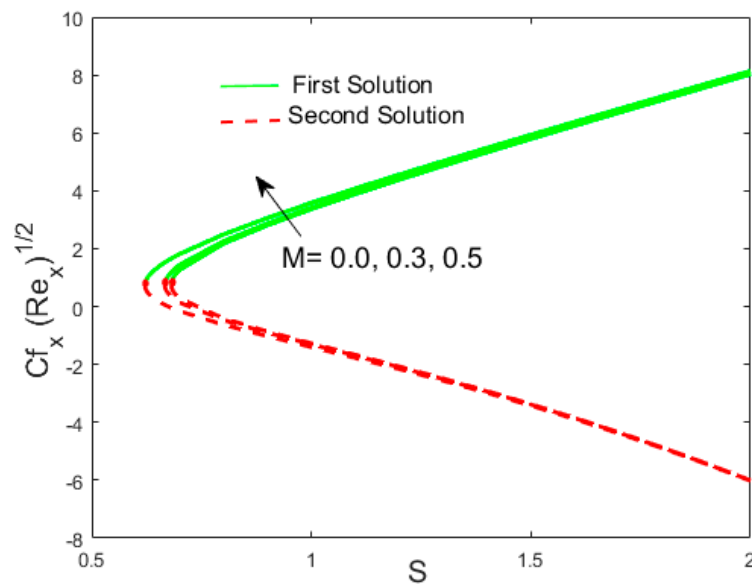


Figure 16. Impact of  $M$  versus  $S$  on  $Cf_x Re_x^{1/2}$ .

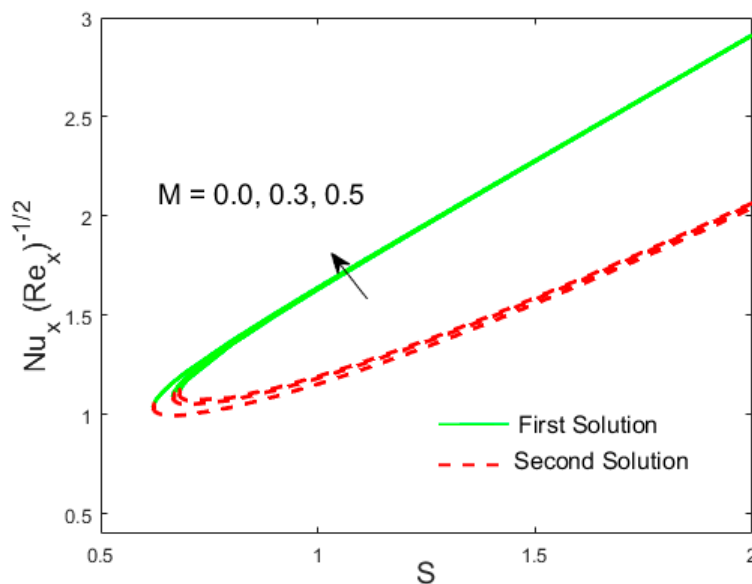


Figure 17. Impact of  $M$  versus  $S$  on  $Nu_x Re_x^{-1/2}$ .

Figures 18 and 19 numerically present the results of the local Nusselt number, which was obtained for dissimilar choices of vigorous physical parameters like  $Ec$  and  $R_d$ . These figures are drawn in contradiction of the parameter  $S$  by keeping all the other several parameters as fixed. In the aforementioned plots, the local Nusselt number decelerates for both branches of solutions due to significant changes in the values of  $Ec$ . The similar result for a local Nusselt number is shown above in Figure 19 for the increment in  $R_d$ . Physically, the values of  $R_d$  suggest the dominance of conduction, and, therefore, the heat transfer rate is reduced while the increment in the  $Ec$  parameter indicates less heat transfer of the liquid compared to the ambient liquid. As an outcome, the rate of the heat transfer decays for both branches of the solutions.

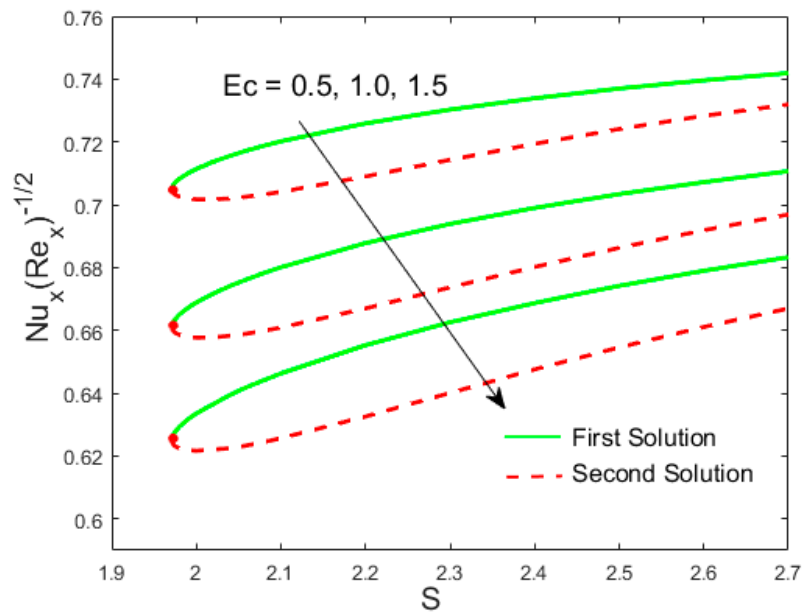


Figure 18. Influence of  $Ec$  versus  $S$  on  $Nu_x Re_x^{-1/2}$ .

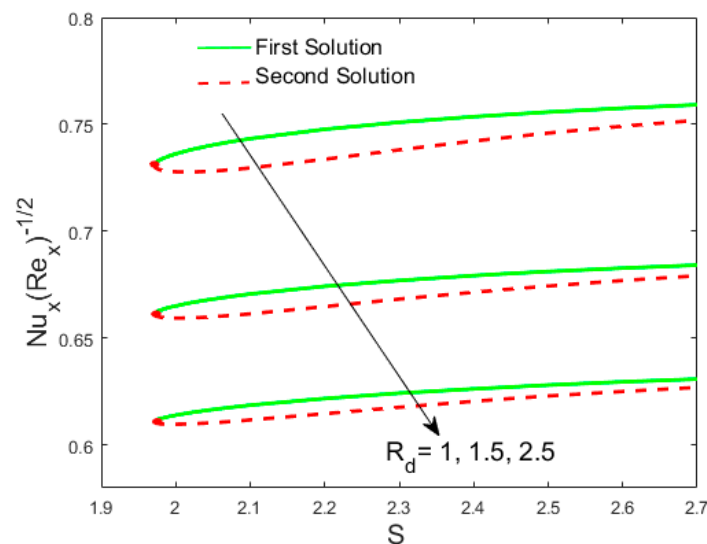


Figure 19. Influence of  $R_d$  versus  $S$  on  $Nu_x Re_x^{-1/2}$ .

### 5. Conclusions

In this study, we investigated the MHD flow problem involving  $MoS_2-SiO_2$  hybrid nanofluids in ethylene glycol (Carreau liquid) and the heat transfer from a nonlinear convectively-heated porous shrinking surface with a nonlinear radiative effect. The dual non-similarity solutions of the transmuted equations were acquired via the `bvp4c` function in Matlab. These multiple non-similarity solutions were used solely for the specific choices of the suction parameters. The velocity and temperature of the nanoliquid were enhanced due to the augmentation of the hybrid nanoparticle in the first solution and the decrease in the second solution. In addition, the velocity of the fluid enhances with larger magnetic parameter for the first solution and decreases for the second solution for the shear thinning liquid along with the shear thickening liquid. While the fluid of the temperature increases for the shear thinning of the liquid and decreases for the shear thickening of the liquid in the first solution, the reverse development is observed in the second solution. The inclusion of the Eckert number and the convective parameter increased the temperature distribution in both the upper and the lower branch solutions, while the temperature distribution declined due to the larger radiation parameter.

Moreover, the Weissenberg number  $We$  decreased the coefficient of the skin friction in the first solution and increased it in the second solution, while the Nusselt number increased due to the higher  $We$  in the first solution; conversely, a conflicting drift was observed in the second solution. The skin friction and the Nusselt number increased for increments in the magnetic parameters in the first solution, while the repeal result was achieved in the second branch solution.

Finally, this research can be extended by considering a mixed convection flow or time dependent flow. It is estimated that the present numerical results will provide significant knowledge for computer routines for more complex problems concerning hybrid nanoliquids in the presence of non-Newtonian base fluids through heated surfaces due to their numerous applications in heat transfer processes, such as in solar collectors, heat exchangers, oil recovery, etc., and also stimulate curiosity for future experimental work.

**Author Contributions:** A.Z. and U.K.; Writing-Original Draft, I.K.; Conceptualization, D.B.; Methodology, I.K.; Software, K.S.N.; Validation, D.B.; Formal Analysis, A.Z.; Writing-Review & Editing, Investigation, D.B.; Resources, I.K. Data Curation, K.S.N.; Visualization and Supervision, D.B.; Project Administration and Funding. All authors have read and agreed to the published version of the manuscript.

**Funding:** This research received no external funding.

**Acknowledgments:** Authors are grateful to editor and referees.

**Conflicts of Interest:** The authors declare no conflict of interest.

## References

- Sarkar, J.; Ghosh, P.; Adil, A. A review on hybrid nanofluids: Recent research, development and applications. *Renew. Sustain. Energy Rev.* **2015**, *43*, 164–177. [[CrossRef](#)]
- Sidik, N.A.C.; Jamil, M.M.; Aziz Japar, W.M.A.; Adamu, I.M. A review on preparation methods, stability and applications of hybrid nanofluids. *Renew. Sustain. Energy Rev.* **2017**, *80*, 1112–1122. [[CrossRef](#)]
- Das, P.K. A Review based on the effect and mechanism of thermal conductivity of normal nanofluids and hybrid nanofluids. *J. Mol. Liq.* **2017**, *240*, 420–446. [[CrossRef](#)]
- Ghadikolaei, S.S.; Yassari, M.; Sadeghi, H.; Hosseinzadeh, K.; Ganji, D.D. Investigation on thermophysical properties of  $TiO_2$ -Cu/ $H_2O$  hybrid nanofluid transport dependent on shape factor in MHD stagnation point flow. *Powder Technol.* **2017**, *322*, 428–438. [[CrossRef](#)]
- Zeeshan, A.; Shehzad, N.; Ellahi, R.; Alamri, S.Z. Convective Poiseuille flow of  $Al_2O_3$ -EG nanofluid in a porous wavy channel with thermal radiation. *Neural. Comput. Appl.* **2018**, *30*, 3371–3382. [[CrossRef](#)]
- Ghadikolaei, S.S.; Hosseinzadeh, K.h.; Ganji, D.D. Investigation on three dimensional squeezing flow of mixture base fluid (ethylene glycol-water) suspended by hybrid nanoparticle ( $Fe_3O_4$ -Ag) dependent on shape factor. *J. Mol. Liq.* **2018**, *262*, 376–388. [[CrossRef](#)]
- Khan, U.; Zaib, A.; Khan, I.; Nisar, K.S. Activation energy on MHD flow of titanium alloy ( $Ti_6Al_4V$ ) nanoparticle along with a cross flow and streamwise direction with binary chemical reaction and non-linear radiation: Dual Solutions. *J. Mater. Res. Technol.* **2019**, *9*, 188–199. [[CrossRef](#)]
- Kumar, V.; Sahoo, R.R. Viscosity and thermal conductivity comparative study for hybrid nanofluid in binary base fluids. *Heat Transf. Asian Res.* **2019**, *48*, 3144–3161. [[CrossRef](#)]
- Wang, C.Y. Liquid film on an unsteady stretching sheet. *Quart. Appl. Math.* **1990**, *48*, 601–610. [[CrossRef](#)]
- Miklavčič, M.; Wang, C.Y. Viscous flow due a shrinking sheet. *Quart. Appl. Math.* **2006**, *64*, 283–290. [[CrossRef](#)]
- Fang, T.; Zhang, J. Closed-form exact solution of MHD viscous flow over a shrinking sheet. *Commun. Nonlinear Sci. Numer. Simul.* **2009**, *14*, 2853–2857. [[CrossRef](#)]
- Khan, Y.; Wu, Q.; Faraz, N.; Yildirim, A. The effects of variable viscosity and thermal conductivity on a thin film flow over a shrinking/stretching sheet. *Comp. Math. Appl.* **2011**, *61*, 3391–3399. [[CrossRef](#)]
- Bhattacharyya, K.; Mukhopadhyay, S.; Layek, G.C. Slip effects on boundary layer stagnation-point flow and heat transfer towards a shrinking sheet. *Int. J. Heat Mass Transf.* **2011**, *54*, 308–313. [[CrossRef](#)]
- Makinde, O.D.; Khan, W.A.; Khan, Z.H. Buoyancy effects on MHD stagnation point flow and heat transfer of a nanofluid past a convectively heated stretching/shrinking sheet. *Int. J. Heat Mass Transf.* **2013**, *62*, 526–533. [[CrossRef](#)]

15. Mahmood, T.; Shah, S.M.; Abbas, G. Magnetohydrodynamics viscous flow over a shrinking sheet in a second order slip flow model. *Heat Transf. Res.* **2015**, *46*, 725–734. [[CrossRef](#)]
16. Mansur, S.; Ishak, A.; Pop, I. The magnetohydrodynamic stagnation point flow of a nanofluid over a stretching/shrinking sheet with suction. *PLoS ONE* **2015**, *10*, e0117733. [[CrossRef](#)]
17. Carreau, P.J. Rheological equations from molecular network theories. *Trans. Soc. Rheol.* **1972**, *116*, 99–127. [[CrossRef](#)]
18. Akbar, N.S.; Nadeem, S.; Haq, R.; Ye, S.W. MHD stagnation point flow of Carreau fluid toward a permeable shrinking sheet: Dual solutions. *Ain Shams Eng. J.* **2014**, *5*, 1233–1239. [[CrossRef](#)]
19. Abbasi, F.M.; Hayat, T.; Alsaedi, A. Numerical analysis for MHD peristaltic transport of Carreau-Yasuda fluid in a curved channel with Hall effects. *J. Magn. Magn. Mater.* **2015**, *382*, 104–110. [[CrossRef](#)]
20. Khan, M.; Hashim. Boundary layer flow and heat transfer to Carreau fluid over a nonlinear stretching sheet. *AIP Adv.* **2015**, *5*, 107203. [[CrossRef](#)]
21. Khan, M.; Hashim; Hussain, M.; Azam, M. Magnetohydrodynamic flow of Carreau fluid over a convectively heated surface in the presence of non-linear radiation. *J. Magn. Magn. Mater.* **2016**, *412*, 63–68. [[CrossRef](#)]
22. Aziz, A. A similarity solution for laminar thermal boundary layer over a flat plate with a convective surface boundary condition. *Commun. Nonlinear Sci. Numer. Simul.* **2009**, *14*, 1064–1068. [[CrossRef](#)]
23. Makinde, O.D.; Aziz, A. MHD mixed convection from a vertical plate embedded in a porous medium with a convective boundary condition. *Int. J. Thermal Sci.* **2010**, *49*, 1813–1820. [[CrossRef](#)]
24. Ishak, A. Similarity solutions for flow and heat transfer over a permeable surface with convective boundary condition. *Appl. Math. Comput.* **2014**, *217*, 837–842. [[CrossRef](#)]
25. Rahman, M.M.; Merkin, J.H.; Pop, I. Mixed convection boundary-layer flow past a vertical flat plate with a convective boundary condition. *Acta Mech.* **2015**, *226*, 2441–2460. [[CrossRef](#)]
26. Ibrahim, W.; Haq, R.U. Magnetohydrodynamic (MHD) stagnation point flow of nanofluid past a stretching sheet with convective boundary condition. *J. Braz. Soc. Mech. Sci. Eng.* **2015**, *38*, 1155–1164. [[CrossRef](#)]
27. Makinde, O.D.; Khan, W.A.; Khan, Z.H. Stagnation point flow of MHD chemically reacting nanofluid over a stretching convective surface with slip and radiative heat. *Proc. Inst. Mech. Eng. Part E J. Process Mech. Eng.* **2017**, *231*, 695–703. [[CrossRef](#)]
28. Maurer, H.; Kessler, C. Identification and quantification of ethylene glycol and diethylene glycol in plasma using gas chromatography-mass spectrometry. *Arch. Toxicol.* **1988**, *62*, 66–69. [[CrossRef](#)]
29. Mariano, A.; Pastoriza-Gallego, M.J.; Lugo, L.; Camacho, A.; Canzonieri, S.; Pineiro, M.M. Thermal conductivity, rheological behaviour and density of non-Newtonian ethylene glycol-based SnO<sub>2</sub> nanofluids. *Fluid Phase Equilib.* **2013**, *337*, 119–124. [[CrossRef](#)]
30. Xie, H.; Jiang, B.; Liu, B.; Wang, Q.; Xu, J.; Pan, F. An investigation on the tribological performances of the SiO<sub>2</sub>-MoS<sub>2</sub> hybrid nanofluids for magnesium alloy-steel contacts. *Nano. Res. Lett.* **2016**, *11*, 329–336. [[CrossRef](#)]
31. Mushtaq, M.; Mustafa, M.; Hayat, T.; Alsaedi, A. Nonlinear radiative heat transfer in the flow of nanofluid due to solar energy: A numerical study. *J. Taiwan Inst. Chem. Eng.* **2014**, *45*, 1176–1183. [[CrossRef](#)]
32. David, R.M. *Introduction to the Theory of Stability*; Springer: Berlin/Heidelberg, Germany, 2012.
33. Weidman, C.R.; Millner, R. High-resolution stable isotope records from North Atlantic cod. *Fish. Res.* **2000**, *46*, 327–342. [[CrossRef](#)]
34. Zaib, A.; Chamkha, A.J.; Rashidi, M.M.; Bhattacharyya, K. Impact of nanoparticles on flow of a special non-Newtonian third-grade fluid over a porous heated shrinking sheet with nonlinear radiation. *Nonlinear Eng.* **2018**, *7*, 103–111. [[CrossRef](#)]
35. Azhar, E.; Maraj, E.N.; Iqbal, Z. Mechanistic investigation for the axisymmetric transport of nanocomposite molybdenum disulfide-silicon dioxide in ethylene glycol and sphericity assessment of nanoscale particles. *Eur. Phys. J. Plus* **2018**, *133*, 130. [[CrossRef](#)]

36. Akbar, N.S.; Iqbal, Z.; Ahmad, B.; Maraj, E.N. Mechanistic investigation for shape factor analysis of SiO<sub>2</sub>/MoS<sub>2</sub>—Ethylene glycol inside a vertical channel influenced by oscillatory temperature gradient. *Can. J. Phys.* **2019**, *97*, 950–958. [[CrossRef](#)]
37. Khan, M.; Sardar, H.; Gulzar, M.M.; Alshomrani, A.S. On multiple solutions of non-Newtonian Carreau fluid flow over an inclined shrinking sheet. *Res. Phys.* **2018**, *8*, 926–932. [[CrossRef](#)]



© 2020 by the authors. Licensee MDPI, Basel, Switzerland. This article is an open access article distributed under the terms and conditions of the Creative Commons Attribution (CC BY) license (<http://creativecommons.org/licenses/by/4.0/>).